



CrossMark  
click for updates

Cite this: *RSC Adv.*, 2015, 5, 63917

# Heteropolyacid generated on the surface of iron phosphate nanotubes: structure and catalytic activity studies†

Ebtesam Al-Mutairi, Katabathini Narasimharao\* and Mohamed Mokhtar\*

Structural and catalytic properties of a Mo based heteropolyacid generated after impregnation of MoO<sub>x</sub> on the surface of porous iron phosphate nanotubes (FeP) were studied. Nano sized MoO<sub>x</sub>-FeP composites with different Mo molar loadings (1–5%) have been prepared under acidic conditions. Synthesized composites were characterised by elemental analysis, X-ray diffraction, transmission electron microscopy, Raman spectroscopy, UV-vis spectroscopy, X-ray photoelectron spectroscopy, acidity measurements using FTIR, N<sub>2</sub>-physisorption and H<sub>2</sub>-temperature programmed reduction methods. Spectroscopic characterization results suggest that Keggin-type FeMoP species were formed on the surface of the iron phosphate nanotubes in the case of catalysts with higher (4 and 5 mol%) Mo loadings. Pure iron phosphate nanotubes, Fe<sub>2</sub>O<sub>3</sub>, MoO<sub>3</sub> and bulk FeMoP HPA samples are less active than MoO<sub>x</sub>-FeP composite samples for the benzylation of benzene with benzyl chloride, particularly the 5 mol% Mo loaded catalyst showed high activity. The enhanced catalytic activity of this catalyst is attributed to the presence of easily reducible, acidic and porous FeMoP heteropolyacid species. These materials can be readily separated from the reaction system for reuse. They are resistant to leaching of the active heteropolyacid species.

Received 11th June 2015

Accepted 21st July 2015

DOI: 10.1039/c5ra11175g

www.rsc.org/advances

## 1 Introduction

The fine chemical industry has experienced tremendous growth over the past few years due to the high demand for products like pharmaceuticals, pesticides, fragrances, flavourings and food additives.<sup>1</sup> The stoichiometric organic synthesis that largely followed so far leaves huge quantities of inorganic salts as by-products, the disposal of which is a serious problem due to keen environmental awareness and tightened regulations.<sup>2</sup> Increased competition in the industry has pushed the research and development activity on fine chemicals toward finding more cost-effective catalytic routes. Diphenylmethane, also known as benzyl benzene, is a valuable intermediate in the chemical industry due to its use in the dye and perfume manufacturing processes.<sup>3</sup> Friedel-Craft type benzylation of benzene using benzyl chloride to afford diphenylmethane is a well-known method of synthesising diphenylmethane. The commonly used homogeneous catalysts, such as AlCl<sub>3</sub>, BF<sub>3</sub>, H<sub>3</sub>PO<sub>4</sub> and H<sub>2</sub>SO<sub>4</sub>, suffer from several disadvantages, including difficulty in separation, recovery, disposal of used catalyst, corrosion and high

toxicity. The development of reusable heterogeneous catalysts has gained practical importance in overcoming the problems associated with homogenous catalysts.<sup>4</sup>

The utilization of solid heteropolyacids (HPAs) as alternate heterogamous catalysts for conventionally used reagents, such as HF, H<sub>2</sub>SO<sub>4</sub> is well known for many years.<sup>5</sup> HPAs are oxoclusters of transition metals, such as W and Mo. It is well known that HPAs are insoluble in non-polar solvents, but highly soluble in polar ones without structure change. Due to their unique combination of acid-base and redox properties, these kinds of solids have been used successfully as solid catalysts in their proton or salt form for acid and redox catalysed reactions.<sup>6</sup>

Thermally stable and high surface area heteropoly acids and salts of heteropoly acids supported on solid metal oxides have been used as catalysts for alkylation and acylation reactions.<sup>7</sup> Kamalakar *et al.*<sup>8</sup> dispersed HPAs on mesoporous silica, such as MCM-41, FSM-16 and SBA-15, by utilising the impregnation method and testing the supported HPA catalysts in the benzylation of benzene and substituted aromatics with benzyl alcohol. Tipnis *et al.*<sup>9</sup> used bulk and supported Fe(III) and Al(III) salts of tungstophosphoric acid catalysts for the benzylation reaction. The authors observed that clay-supported Fe salt of tungstophosphoric acid showed the highest activity for the reaction, resulting in the complete conversion of benzyl chloride in 60 minutes with a selectivity of 98.7% towards diphenylmethane, however, leaching of active heteropolyacid catalyst is a problem.

Department of Chemistry, Faculty of Science, King Abdulaziz University, P. O. Box 80203, Jeddah 21589, Saudi Arabia. E-mail: nkatabathini@kau.edu.sa; katabathini@yahoo.com; mmokhtar2000@yahoo.com; Fax: +966-26952292; Tel: +966-538638994, +966-500558045

† Electronic supplementary information (ESI) available. See DOI: 10.1039/c5ra11175g

Literature reports revealed that due to ionic interactions between the support surface and HPA clusters are responsible in generation of the active species, however, due to weak nature of interaction, it is possible for HPA clusters to leach out from the support during reactions in solvents.<sup>10</sup> Previously, we have synthesised the ammonium salt of molybdophosphoric acid on the surface of niobium phosphate by using a novel *in situ* method of preparation.<sup>11</sup> In this method, the phosphate ions on the support were made to react *in situ* with the ammonium heptamolybdate in the solution under acidic conditions. Subsequently, the heteropoly Keggin ions were grown at specific sites on the support.

In the present work, we prepared a series of porous nano-composite of MoO<sub>x</sub>-FeP catalysts with different Mo loadings to generate HPA on the surface of iron phosphate nanotubes. The synthesised materials were used as catalysts for the benzylation of benzene using benzyl chloride. A systematic characterisation was performed to study the physico-chemical properties of the catalysts. An effort was made to correlate the benzylation activity of the catalysts with their physico-chemical properties.

## 2 Experimental

### 2.1 Preparation of materials

**2.1.1 Porous iron phosphate nanotubes.** Porous iron phosphate nanotubes were prepared by following the method reported.<sup>12</sup> In a typical method, 4.0 g of ferric nitrate was dissolved in 20 mL of distilled water and 9.0 g mono-hydrogen sodium phosphate was dissolved in 60 mL of distilled water. The two solutions were mixed under vigorous stirring to obtain a precipitate. The obtained precipitate was recovered by centrifugation and was suspended in 10 mL of aqueous solution contained 2.88 g sodium dodecyl sulfate. Then, 1.8 mL hydro-fluoric acid (40 wt%) was dropped into the suspension with vigorous stirring. The resulting transparent solution was continuously stirred at room temperature for 24 h and then soaked at 60 °C for 12 h. After cooling to room temperature, a light yellow precipitate was observed in the solution and precipitate was recovered by centrifugation. The obtained precipitate was washed with water for four times and then acetone and drying at 100 °C. The dried solid was suspended in absolute ethanol and subjected to hydrothermal treatment in a Teflon-lined autoclave at 150 °C for 24 h. Then, the resultant precipitate was recovered by centrifugation, followed by washing with ethanol and dried 100 °C. The dodecyl sulfate surfactant was removed by thermal treatment at 500 °C for 4 h in air and the resultant sample was denoted as FeP.

**2.1.2 Synthesis of MoO<sub>x</sub>-FeP nanocomposites.** A series of catalysts were prepared with different Mo loadings over the range of 1 to 5 mol%. Simple impregnation method was employed and it involved the dissolution of required amount of ammonium molybdate (Aldrich 99%) in 20 mL distilled water in a round-bottomed flask, followed by the addition of the porous FeP support. The pH of the contents was maintained at 2 by adding the diluted HCl solution. The resulting mixture was left overnight followed by evaporation to a dry, free flowing powder at 60 °C under vacuum was obtained. Finally, the catalysts were

thermally treated at 300 °C for 4 h, and were stored in air prior to analysis and reaction testing. The following nomenclature was applied for the sample codes: xMo-FeP, wherein 'x' represents the amount of Mo loading and FeP represents 'iron phosphate'. FePMo<sub>12</sub>O<sub>40</sub> heteropolyacid salt (FePMo) was synthesized using the methodology reported in ref. 9 to its activity against that Mo-FeP catalysts.

### 2.2 Characterization of synthesised materials

The elemental composition of the materials was determined using inductively coupled plasma mass spectrometry (ICP-MS), Optima 7300DV, Perkin Elmer Corporation, USA. X-ray powder diffraction (XRD) studies were performed for all of the prepared solid samples using a Bruker diffractometer (Bruker D8 advance target). The patterns were run with copper K $\alpha$  and a monochromator ( $\lambda = 1.5405 \text{ \AA}$ ) at 40 kV and 40 mA. The particle size of the catalyst was calculated using Scherrer's equation:

$$D = B\lambda/\beta_{1/2} \cos \theta \quad (1)$$

where  $D$  is the average crystallite size of the phase under investigation,  $B$  is the Scherrer constant (0.89),  $\lambda$  is wavelength of the X-ray beam used (1.54056 Å),  $\beta_{1/2}$  is the full width at half maximum (FWHM) of the diffraction peak and  $\theta$  is the diffraction angle. Identification of the different crystalline phases in the samples was performed by comparing the data with the Joint Committee for Powder Diffraction Standards (JCPDS) files.

The Raman spectra of samples were measured with a Bruker Equinox 55FT-IR spectrometer equipped with a FRA106/SFT-Raman module and a liquid N<sub>2</sub> cooled Ge detector, using the 1064 nm line of an Nd:YAG laser with an output laser power of 400 mW. A 200 kV Philips CM200FEG microscope equipped with a field emission gun was used for transmission electron microscopy (TEM) analysis. The coefficient of the spherical aberration was  $C_s = 1.35 \text{ mm}$ . The information limit was better than 0.18 nm. High resolution images with a pixel size of 0.044 nm were taken with a charge-coupled device (CCD) camera. The textural properties of the prepared samples were determined from nitrogen adsorption/desorption isotherm measurements at -196 °C using the model Autosorb-1 surface analyser, Quantachrome. Prior to measurement, each sample was degassed for 6 h at 150 °C. The specific surface area,  $S_{\text{BET}}$ , was calculated by applying the Brunauer-Emmett-Teller (BET) equation. The average pore radius was estimated from the relation  $2V_p/S_{\text{BET}}$ , where  $V_p$  is the total pore volume (at  $P/P^0 = 0.975$ ). Pore size distribution over the mesopore range was generated through the Barrett-Joyner-Halenda (BJH) analysis of the desorption branches. Then, the values for the average pore size were calculated.

FTIR spectra of calcined catalysts obtained at room temperature using Perkin-Elmer Spectrum 100 FTIR spectrometer. Then, the samples were subjected to pyridine adsorption analysis. The analysis was carried out over a catalyst disk which was treated under vacuum for 5 h. Later, the samples were treated with pyridine vapor and finally heated at 100 °C under vacuum for 30 min. The amount of Brønsted and Lewis acid

sites was calculated *via* integration of the area of the absorption bands showing the maximum values of intensity at  $1446\text{ cm}^{-1}$  and  $1536\text{ cm}^{-1}$ , respectively. Integrated absorbance of each band was obtained using the appropriate software by applying the corresponding extinction coefficient and normalized by the weight of the samples.

The XPS measurements were carried out using a SPECS GmbH X-ray photoelectron spectrometer. Prior to analysis, the samples were degassed under vacuum inside the load lock for 16 h. The binding energy of the adventitious carbon (C 1s) line at 284.6 eV was used for calibration and the positions of other peaks were corrected according to the position of the C 1s signal. For the measurements of the high resolution spectra, the analyser was set to the large area lens mode with energy steps of 25 meV and in Fixed Analyser Transmission (FAT) mode with pass energies of 34 eV and dwell times of 100 ms. The photoelectron spectra of the four samples were recorded with the acceptance area and angle of 5 mm in diameter and up to  $5^\circ$ , respectively. The base pressure during all measurements was  $5 \times 10^{-9}$  mbar. A standard dual anode excitation source with Mg K $\alpha$  (1253.6 eV) radiation was used at 13 kV and 100 W. H<sub>2</sub>-TPR patterns of the samples were recorded using CHEMBET-3000 (Quantachrome, USA) instrument. TPR experiments were carried out in a quartz reactor; 100 mg of catalyst sample was loaded into reactor, thermally treated at 120 °C for 2 hours and cooled to 30 °C under the flow of helium gas and then the sample is heated from 30 to 800 °C at the rate of  $5\text{ }^\circ\text{C min}^{-1}$  under the flow of 90% helium–10% hydrogen (by volume) gas at flow rate of  $60\text{ mL min}^{-1}$ . The effluent hydrogen concentration was detected by the thermal conductivity detector (TCD).

### 2.3 Benzylolation of benzene using benzyl chloride

The liquid phase benzylolation of benzene with benzyl chloride (BC) was carried out in a three necked round-bottomed flask equipped with a reflux condenser and electrically heated in a precisely controlled oil bath under atmospheric pressure. In a typical run, 13 mL of benzene was added to 50 mg catalyst (which had been activated overnight at 100 °C). The reaction mixture was maintained for 30 min at the required reaction temperature and then 1 mL of benzyl chloride was added. The moment was regarded as initial reaction time. Liquid samples were withdrawn at regular intervals and analysed using gas chromatography (HP-6890) equipped with a flame ionisation detector (FID) and HP-5 capillary column. The products were also identified by gas chromatography-mass spectrometry (GC-MS, HP-5975C) analysis. Since benzene was in excess, conversion was calculated based on the benzylating reagent (*i.e.*, BC). Selectivity to the product diphenylmethane (DPM) was expressed as the amount of the particular product divided by the amount of the total products and multiplied by 100.

## 3 Results and discussion

### 3.1 Powder X-ray diffraction

Powder X-ray diffraction (XRD) analysis was used to determine the phase purity of the samples. The XRD patterns of pure FeP

and Mo–FeP samples are shown in Fig. 1. Pure FeP sample showed diffraction peaks of FePO<sub>4</sub> indexed from the standard diffraction peaks [JCPDF file no. 29-0715], indicating that the crystal structure is a hexagonal system with space group *P*321. Diffraction peaks related to phase impurities were not observed in the XRD pattern, confirming the high purity of the FePO<sub>4</sub> nanotubes.

The observed broad diffraction pattern of the FeP sample revealed the nanosize nature of the solid material. The XRD patterns of the MoO<sub>x</sub> deposited FeP solids also showed only pure FePO<sub>4</sub> phase with hexagonal structure. There were no diffraction peaks observed due to MoO<sub>3</sub> or any species due to interaction between FePO<sub>4</sub> and MoO<sub>x</sub>. This is possibly due to either fine dispersion of supported Mo species on the surface of FeP or the phase formation might be under 5%, which is the minimum X-ray detection limit. However, it is interesting to note that the diffraction peaks of MoO<sub>x</sub> deposited FeP samples are more intense and narrower than that of the pure FeP sample, indicating that the MoO<sub>x</sub> deposited samples are more crystalline than pure FeP.

The intensity of the diffraction peaks of FePO<sub>4</sub> changed with change of the Mo mol%, confirming the role of MoO<sub>x</sub> in the enhancement of the transformation of the partially crystalline FeP nanotubes. To understand the role of MoO<sub>x</sub> role in enhancement of crystallinity of Mo–FeP samples, a FeP sample was prepared by subjecting it to all the post treatments similar to preparation of Mo–FeP, but without addition of Mo. The XRD pattern of this sample was presented in the ESI.† The XRD pattern of this sample showed a small improvement in the crystallinity of the sample, when it compared to crystallinity of pure FeP, but not as significant as observed in the Mo–FeP samples. This observation indicating that both Mo addition and the post treatment conditions are affecting the crystallinity of the Mo–FeP samples. A possible dispersion or incorporation of MoO<sub>x</sub> species on the surface or bulk of FeP was studied using the XPS technique and the results are discussed in the later part of this section.

The average crystallite sizes of the FeP and 5 mol% Mo deposited sample are 25 nm and 40 nm (Table 1), respectively,

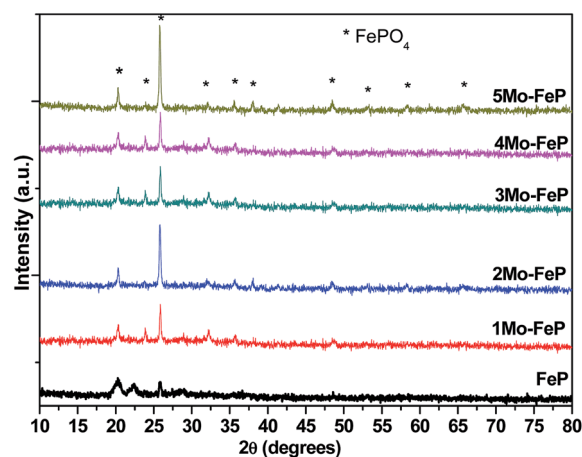


Fig. 1 Powder XRD patterns of FeP and Mo–FeP samples.

and are estimated from the (212) reflection based on the Scherrer eqn (1). The crystallite sizes of the  $\text{MoO}_x$  deposited samples determined using XRD analysis are bigger than observed in TEM images. This might be due to the formation of another phase (amorphous or highly dispersed or under the detection of XRD limit) during the impregnation of the  $\text{MoO}_x$  in acidic solution.

Fig. 2 shows TEM images of the pure FeP and representative  $\text{MoO}_x$  impregnated FeP catalysts. The pure FeP sample possesses mainly tubular structures with diameters of 25–30 nm and lengths of several microns. The walls of the nanotubes range from 4 to 6 nm in thickness. The samples, which contained 1 mol% and 4 mol% of Mo, showed particulates apart from the nanotubes as shown in Fig. 2(b) and (c). The increase of Mo molar loading to 5% resulted in the change of the tubular morphology into wormlike and spherical Keggin structures with meso and macro size voids [Fig. 2(d)]. TEM analysis clearly showed that there are different morphologies for Mo–FeP samples, which is leading to different intensities and reflection broadenings in XRD patterns.

Raman spectra of pure FeP and  $\text{MoO}_x$  impregnated FeP catalysts are shown in Fig. 3(A). The pure FeP sample exhibited two major Raman vibrations at 1010 and 1053  $\text{cm}^{-1}$  along with minor vibrations at 408, 440, 595, 665 and 1166  $\text{cm}^{-1}$ . It was reported that the stretching and bending vibrations of phosphate groups appear in the range of 1000–1200 and 400–700  $\text{cm}^{-1}$ , respectively.<sup>13</sup> The major Raman vibrations at 1010 and 1053  $\text{cm}^{-1}$  can be attributed to alternatively connected tetrahedral  $\text{FeO}_4$  and  $\text{PO}_4$  groups, respectively.<sup>14</sup>

The vibrations at 1167 and 665  $\text{cm}^{-1}$  can be ascribed to the presence of metal phosphate groups. The Mo–FeP catalysts showed new vibrations at 988, 876 and 608  $\text{cm}^{-1}$ , which corresponds to  $\nu_s(\text{Mo}=\text{O}_d)$ ,  $\nu_{as}(\text{M}-\text{O}_b-\text{M})$  and  $\nu_s(\text{Mo}-\text{O}_c-\text{M})$  due to the characteristic of the Keggin anion.<sup>15</sup> It is clear from the Raman data that Keggin type HPA formation is taking place with stoichiometric phosphorous presented in the FeP support.

Fig. 3(B) shows the UV-vis absorption spectra extending from 200 to 800 nm of the FeP and  $\text{MoO}_x$  impregnated FeP samples. The pure FeP sample showed a sharp absorbance bands at around 230 nm and a broad band at around 280 nm, which could be attributed to the P–O and Fe–O charge transfer

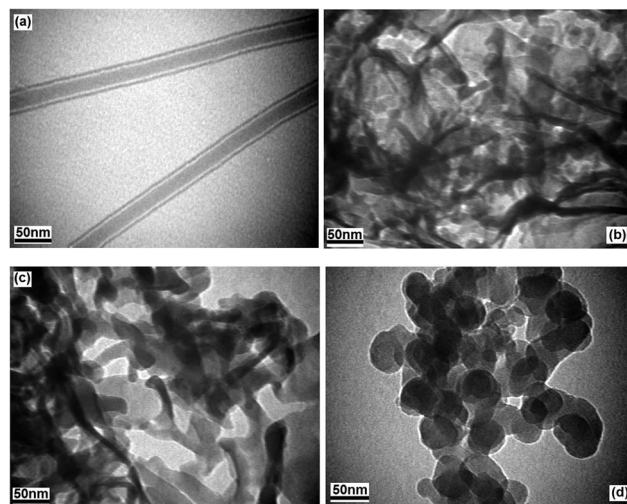


Fig. 2 TEM images of (a) FeP (b) 1Mo–FeP (c) 4Mo–FeP (d) 5Mo–FeP.

transitions, respectively.<sup>14–16</sup> For the  $\text{MoO}_3$  impregnated FeP samples, a new broad absorbance band at higher wavelength (around 370 nm) was observed along with peaks due to FeP indicating that the local structure of the  $\text{MoO}_x$  impregnated FeP samples differed from that of the FeP to some extent. The samples with Mo content from 1 to 4 mol% showed very similar absorption spectrum with a very broad ultraviolet absorption extending from 200 to 400 nm. The strong band centered around 370 nm showing the presence of octahedrally coordinated Mo species in Mo–FeP samples.<sup>17</sup> Further increase of Mo content to 5 mol%, the UV-vis spectrum showed a sharp absorption peak at 310 nm, which could be due to formation of bulk HPA species. The material with different Mo composition is expected to favour different oxidation states for molybdenum species.<sup>18</sup> From these results, it appears that the FeP support is required between 4 and 5% Mo loading to form bulk type heteropolyacid species. In our previous publication,<sup>19</sup> we studied the variation in surface W content as a function of bulk tungsten loading in case of  $\text{WO}_3$ –ZrP composite. The surface W coverage rose continuously as a function of bulk content, with a slight plateau obtained around 5 wt% W, followed by a rapid rise for bulk loadings in excess of 10 wt% W. This variation is suggestive of in-pore adsorption of  $\text{WO}_x$  species for low loadings, with the onset of multilayer/crystalline growth occurring at higher loadings. A very similar phenomenon can be expected in case of  $\text{MoO}_x$ –FeP.

X-ray photoelectron spectroscopy analysis of the samples was performed to investigate the nature of the surface species. The Fe 2p XPS core spectra for all the samples are shown in Fig. 4(A) and deconvoluted Fe 2p XPS spectrum for 5Mo–FeP sample was also depicted at the bottom of the figure. Fe  $2p_{3/2}$  binding energies in the range of 711.1–711.5 eV were observed for FeP and  $\text{MoO}_x$  deposited FeP samples. Alptekin *et al.*<sup>20</sup> observed a binding energy of 712.5 eV for pure FeP and Wang *et al.*<sup>21</sup> reported a value of 713.2 eV for the same material. The binding energies of the Fe  $2p_{1/2}$  and Fe  $2p_{3/2}$  peaks attributed to  $\text{Fe}^{3+}$  in pure FeP are 724.4 eV and 711.5 eV, respectively. A small

Table 1 Crystallite size of catalysts determined from XRD and TEM measurements

S. no.	Catalyst	Crystallite size (nm)	
		XRD	TEM
1	FeP	25	25 <sup>a</sup>
2	1Mo–FeP	29	26 <sup>a</sup>
3	2Mo–FeP	33	28 <sup>a</sup>
4	3Mo–FeP	35	29 <sup>a</sup>
5	4Mo–FeP	38	30 <sup>a</sup>
6	5Mo–FeP	40	32 <sup>b</sup>

<sup>a</sup> Diameter of tubes or worm shape particles. <sup>b</sup> Diameter of spherical particles.

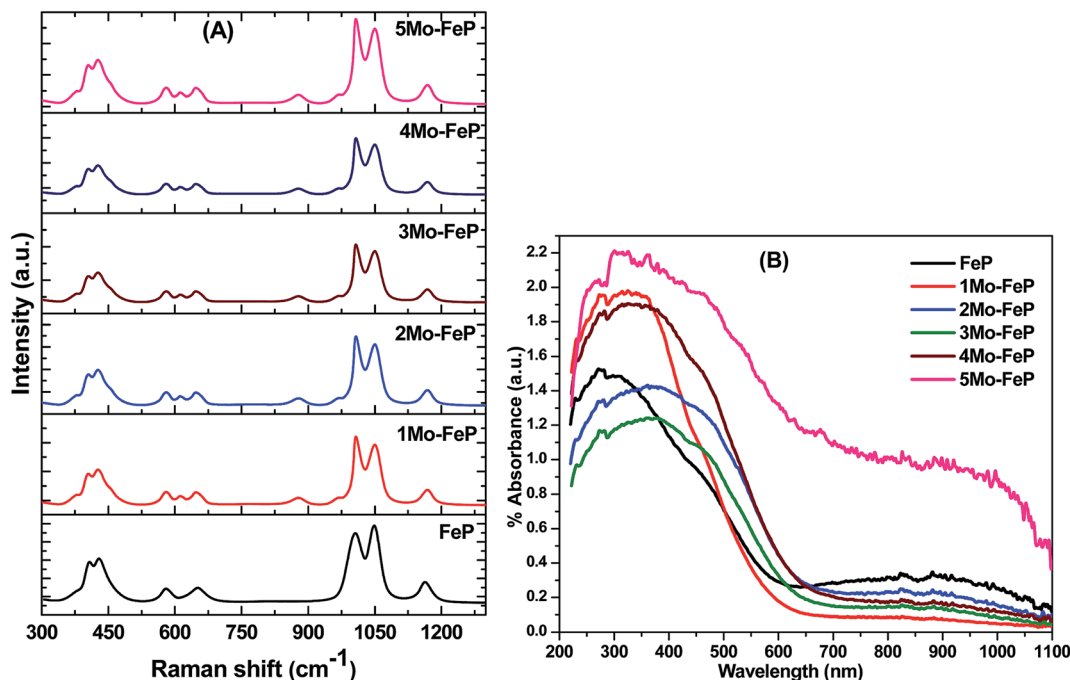


Fig. 3 (A) Raman (B) UV-vis absorption spectra of FeP and Mo-FeP samples.

shift in the binding energies of the Fe 2p peaks in the MoO<sub>x</sub> deposited FeP samples was observed. The deconvoluted Fe 2p<sub>3/2</sub> spectra for 5Mo-FeP sample showed two peaks centred at 711 eV and 712.8 eV due to Fe<sup>3+</sup> species. It is interesting to note that a new small peak appeared at 714 eV in the XPS spectrum of 5Mo-FeP sample. Appearance of a new peak with 2.5 eV binding energy difference for the 5Mo-FeP sample relative to bulk FeP is high enough to attribute this peak to the surface oxidation state of iron between three and two, which is possibly due to FeMoP HPA species.

The Mo 3d XPS core spectra for all the samples are shown in Fig. 4(B). The FeP, 1Mo-FeP and 2Mo-FeP samples did not show any defined Mo 3d contributions. Specifically, 1Mo-FeP and 2Mo-FeP samples did not show any contributions of surface Mo species, probably due to the fact that the actual concentration is very small and the deposited Mo atoms entered into the framework of FeP. In contrast, the 3Mo-FeP and 4Mo-FeP samples showed two broad peaks centred at 231.1 eV. Meanwhile, 232 eV correspond to Mo<sup>6+</sup> (3d<sub>3/2</sub>) and Mo<sup>5+</sup> (3d<sub>5/2</sub>), respectively.<sup>22</sup> However, in the case of the 5Mo-FeP catalyst, the broadness of the peaks disappeared and a doublet Mo 3d<sub>5/2</sub> and 3d<sub>3/2</sub> peaks at 231.3 eV and 235.5 eV was observed. These two species can be attributed to typical Mo<sup>6+</sup> species.<sup>23</sup> Presence of reduced Mo ions was not observed in case of 4Mo-FeP and 5Mo-FeP samples. The binding energy values for all low Mo loading samples are approximately the same, probably due to the presence of Mo with the low oxidation state (5+) in these samples. These results provide evidence that the Keggin type species were formed in case of the 4Mo-FeP and 5Mo-FeP samples, although the Mo ions were placed in a distorted octahedral environment of oxide ions.<sup>24</sup> The O 1s peak for pure FeP at 531 eV [Fig. 4(C)] is attributed to the Fe-O-P bond and

the absence of a characteristic O 1s peak of iron oxide (Fe-O) bond at 530 eV,<sup>25</sup> indicating that the Fe cations are bound as phosphates and not as iron oxides. Deconvoluted spectrum of 5Mo-FeP sample clearly showed a shoulder peak at 531.5 eV. This peak can be attributed to the bridging of the oxygen P-O-P contribution.

The binding energy value observed in all the samples for P 2p<sub>3/2</sub> XPS peak [Fig. 4(D)] is around 132 eV and this peak can be assigned to P with an oxidation state of 5+.<sup>26</sup> The XPS analysis of the FePO<sub>4</sub> showed a peak at 133.8 eV for P 2p<sub>3/2</sub>. The binding energies for the mixture of FePO<sub>4</sub> and MoO<sub>3</sub> provided very similar value for P as the FePO<sub>4</sub> material. The surface atomic Mo/P and Fe/P ratios were calculated and at lower loadings, the Fe/P ratio is identical to that observed for pure FePO<sub>4</sub>.<sup>20</sup> A low surface enrichment of Mo becomes evident as the Mo loading level goes up (Table 2). It appears that Mo is interacting with specific sites on the FeP surface and that the Mo atoms are sorbed or bonded on top of the FeP. As noted above, procedures similar to those employed here significantly overestimate the absolute value of the surface P to the metal ratio.<sup>27</sup> The trend of the surface Mo enrichment, with increasing Mo loading was clearly observed.

The bulk elemental composition of the catalysts was performed using ICP-MS analysis. The calculated percentages of the elements Fe, Mo and P are given in Table S1 (ESI<sup>†</sup>). The results indicate that P/Fe mole ratio of the calcined FeP sample is very close to the stoichiometry of FePO<sub>4</sub>, while the P/Fe mole ratio of MoO<sub>x</sub> deposited samples changed as expected. Considering the P/Fe and P/Mo mole ratios of samples and the difference among them, we can notice that a reaction took place between MoO<sub>x</sub> and FePO<sub>4</sub> during the impregnation in the acidic solution.

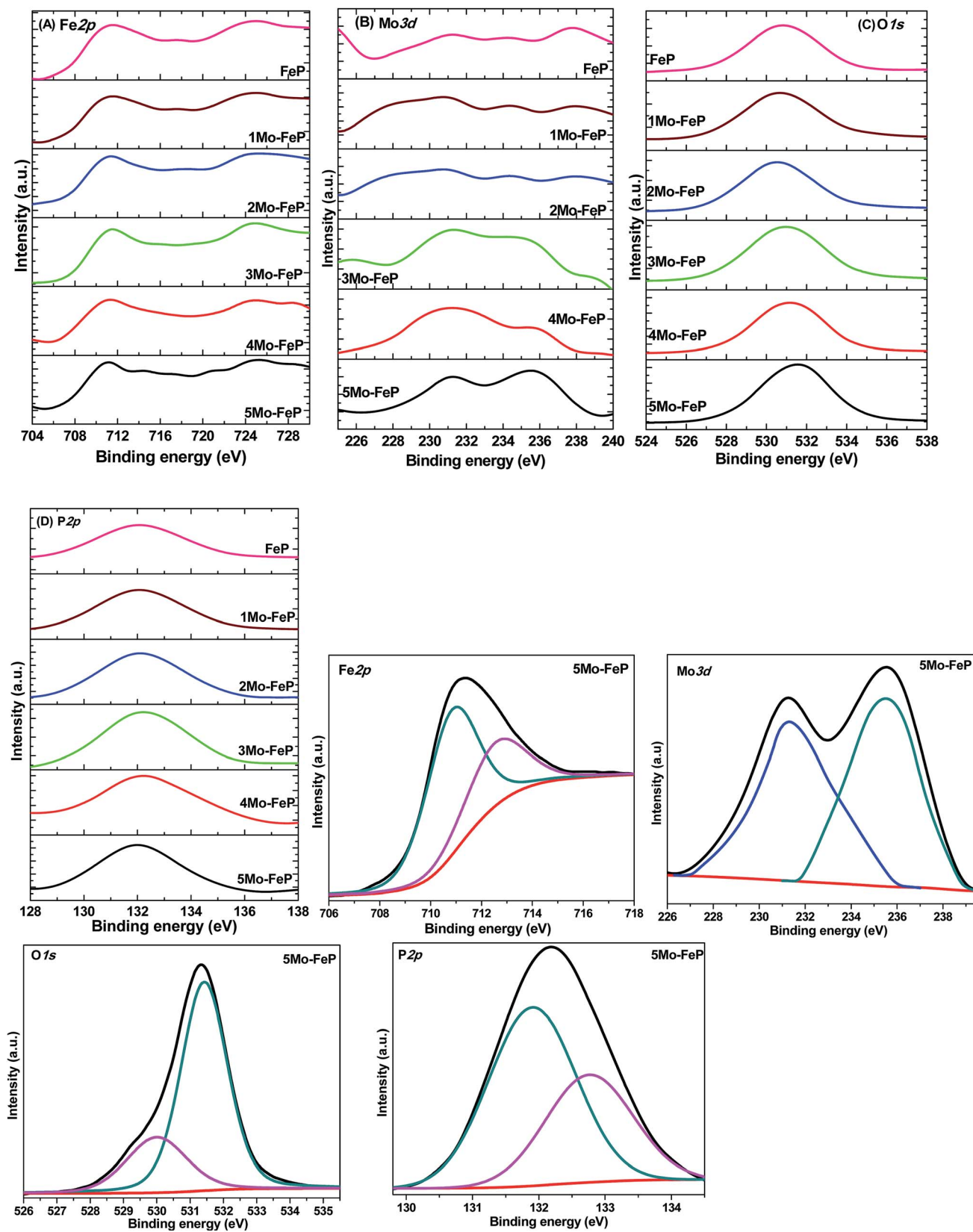


Fig. 4 XPS core spectra for all the samples (A) Fe 2p (B) Mo 3d (C) O 1s (D) P 2p and the deconvoluted spectra for 5Mo-FeP sample.

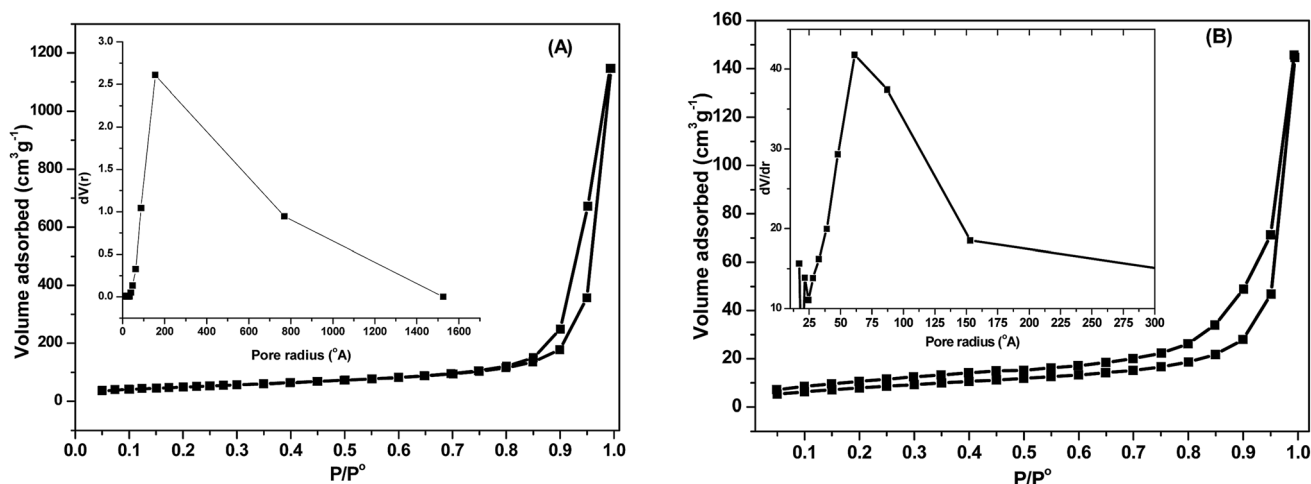
Table 2 Textural properties of catalysts from N<sub>2</sub>-physorption and chemical composition of catalysts from XPS analysis

Catalyst	$S_{\text{BET}}$ (m <sup>2</sup> g <sup>-1</sup> )	$V_p$ (cm <sup>3</sup> g <sup>-1</sup> )	Av. pore diameter (nm)	XPS chemical analysis (molar percent)			
				Mo	Fe	P	O
FeP	123	0.294	20.0	0.0	36.5	20.0	43.5
1Mo-FeP	107	0.254	16.8	0.1	36.4	20.1	43.4
2Mo-FeP	91	0.219	13.0	0.2	36.2	20.1	43.5
3Mo-FeP	76	0.188	12.3	1.4	36.1	20.2	42.3
4Mo-FeP	58	0.171	10.8	2.5	36.1	20.1	41.3
5Mo-FeP	39	0.155	7.5	3.6	35.8	20.0	40.6

Fig. 5(A) and (B) shows the typical N<sub>2</sub> adsorption-desorption isotherms (inset; corresponding pore size distribution) of FeP and 5Mo-FeP samples respectively. The samples are possessed type-IV isotherm with narrow hysteresis loop which indicates the presence of mesopores related to inter-particle voids as defined by the International Union of Pure and Applied Chemistry (IUPAC).<sup>28</sup> Accordingly, the pore size distribution pattern displays a unimodal shape pores with maximum pore radius at 200 Å for FeP and 75 Å for the 5Mo-FeP samples, respectively.

The mesoporous nature observed from the results of the N<sub>2</sub>-physorption is consistent with the pores visualized in the TEM analysis, indicating that the mesopores were raised from the morphology of the FeP nanotubes or Mo-FeP particles. Quantitative calculation shows that pure FeP possesses Brunauer, Emmet and teller (BET) surface area of 123 m<sup>2</sup> g<sup>-1</sup> and a pore volume of 0.294 cm<sup>3</sup> g<sup>-1</sup>. A pronounced decrease of surface area, pore volume and pore diameter were observed with the Mo loading over FeP. The sample with 5 mol% Mo loading possessed surface area, pore volume and pore diameter of 39 m<sup>2</sup> g<sup>-1</sup>, 0.155 cm<sup>3</sup> g<sup>-1</sup> and 7.5 nm, respectively (Table 2). The decrease in the values of the textural properties with the increase in Mo loading is not only due to the formation of Keggin type FePMo heteropolyacid species, but also due to complete transformation of the initial FeP particle morphology.

Temperature programmed reduction (TPR) profiles were recorded for all the samples to determine the reduction temperatures for all the samples [Fig. 6]. Pure FeP exhibited one broad asymmetric reduction peak centred at 700 °C. In comparison to the pure FeP sample, peak position was not changed after the deposition of 1% Mo. However, a low, intense broad peak at 550 °C appeared due to the reduction of the Mo species. Approximately 2Mo-FeP and 3Mo-FeP samples underwent reduction by hydrogen at higher temperatures, showing modified valence stability of the Fe in the FeP nano-material. It was reported that the reduction temperature were 690 °C for FePO<sub>4</sub>, 900 °C for MoPO<sub>4</sub> and 640 °C, 690 °C, 730 °C and 790 °C for the mixture of FePO<sub>4</sub> and MoO<sub>3</sub>.<sup>29</sup> The difference in the reduction temperature in the MoO<sub>x</sub> deposited FeP samples and the broadening of the peaks suggest a chemical interaction between the FePO<sub>4</sub> and MoO<sub>x</sub> in the MoO<sub>x</sub> deposited FeP samples during the reduction. It is interesting that the reduction peak remarkably shifted to lower temperatures for the 4% and 5% Mo loaded samples. As the loading amount reached 5 Mo mol%, the main peak shifted to 675 °C and the shoulder peak appeared distinctly. The major peak at 675 °C and 700 °C probably arose from the reduction of the crystalline FePO<sub>4</sub>. These results strongly suggest that the Keggin type Mo species encapsulated within the mesopore channels of FeP can be reduced at lower temperatures as compared with the crystalline FeP.

Fig. 5 N<sub>2</sub> adsorption-desorption isotherms of (A) FeP (B) 5-MoFeP (inset pore size distribution).

As previously mentioned, the goal of this research is to synthesize the heteropolyacids by interaction of Mo with iron phosphate nanotubes and it is important to study the acidity of the synthesized Mo–FeP catalysts. FTIR spectra of samples after pyridine adsorption at 100 °C followed by evacuation at the same temperature was shown in Fig. 7. It is known that pyridine adsorbed samples exhibit peaks at 1446, 1486 and 1536  $\text{cm}^{-1}$ . The peaks at 1446 and 1536  $\text{cm}^{-1}$  are characteristic of Lewis-coordinated pyridine (L) and Brønsted coordinated pyridine (B) respectively. The band at 1486  $\text{cm}^{-1}$  is due to Lewis and Brønsted coordinated pyridine (L + B).<sup>30</sup> The pure FeP sample showed a small peak at 1486  $\text{cm}^{-1}$ , which is due to minor contribution of Lewis and Brønsted acid sites. However, a major difference was noticed in FTIR spectra MoO<sub>x</sub> impregnated FeP samples, particularly in 5Mo–FeP and 4Mo–FeP samples. The formation of new Lewis sites was clearly observed as revealed by the intense band at 1446  $\text{cm}^{-1}$  along with the peak due to Lewis and Brønsted acid sites.

The Lewis acid sites density for all the catalysts was determined. Pure FeP sample possessed total acid sites density of 0.9, however after impregnation of MoO<sub>x</sub> resulted increase of density of acid sites. A gradual increase of acidity was observed from 1 to 3 mol% (1Mo–FeP = 4.5, 2Mo–FeP = 6.2, 3Mo–FeP = 8.9) and further increasing of Mo loading did not change the density of acid sites (4Mo–FeP = 15.2, 5Mo–FeP = 16.1). The surface species responsible for acidity in these samples are coordinated unsaturated metal ions (Fe<sup>3+</sup> and Mo<sup>5+</sup> ions). These cations possess an uncompensated positive charge and coordinate molecules with a free electron pair and act as Lewis acid sites.<sup>31</sup>

### 3.2 Benzylation of benzene

Benylation of benzene was used as a model reaction to check the capability of the synthesized Mo–FeP materials as redox catalysts. Benzylation of benzene (1), with benzyl chloride (2) as an alkylating agent, produces mainly diphenylmethane (3) (Scheme 1). It is known that Friedel–Crafts reaction is always

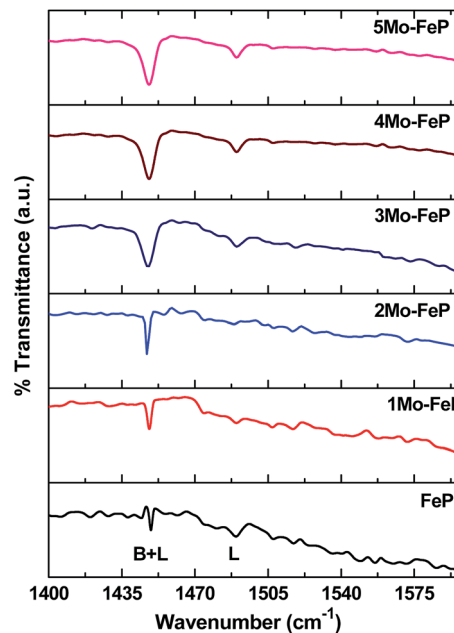


Fig. 7 FTIR spectra of samples after pyridine adsorption.

accompanied by di- and poly-alkylations. The benzylation can also produce dibenylation products (4, 5 and 6) as side products.<sup>1</sup> Thus, dibenzylbenzene, tribenzylbenzene and other side products can be formed in the reaction, with dibenzylbenzene being the most prominent side product.

The conversion of benzyl chloride with reaction time over FeP and MoO<sub>x</sub> impregnated FeP catalysts at 80 °C is shown in Fig. 8(A). As observed, pure FeP offered very low catalytic activity, with a benzyl chloride conversion of 4% after a reaction time of 240 min an increase in the conversion of benzyl chloride (50%) was observed upon the addition of 1 mol% Mo on FeP.

A significant increase of activity was observed after loading 2 mol% Mo on FeP, where 24% of the conversion of benzyl

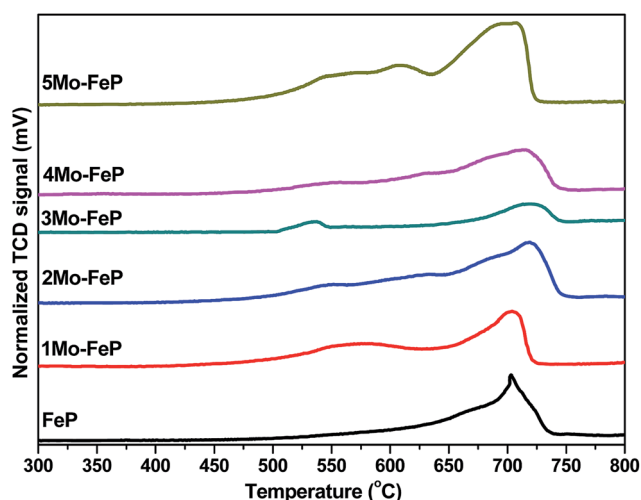
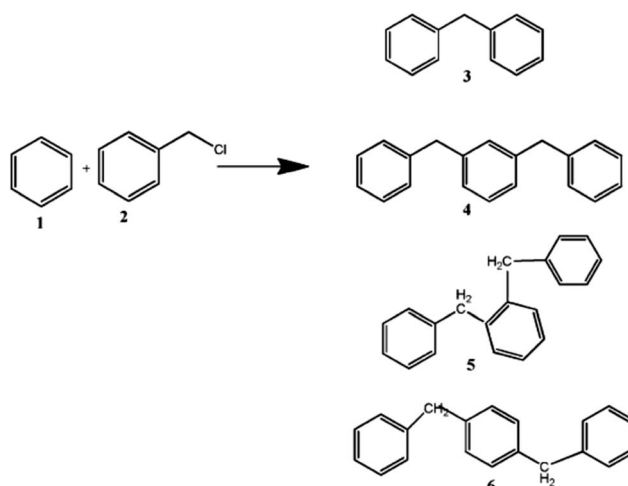


Fig. 6 H<sub>2</sub>-TPR patterns for FeP and Mo–FeP samples.



Scheme 1 Reaction pathway of benzylation of benzene with benzyl chloride.

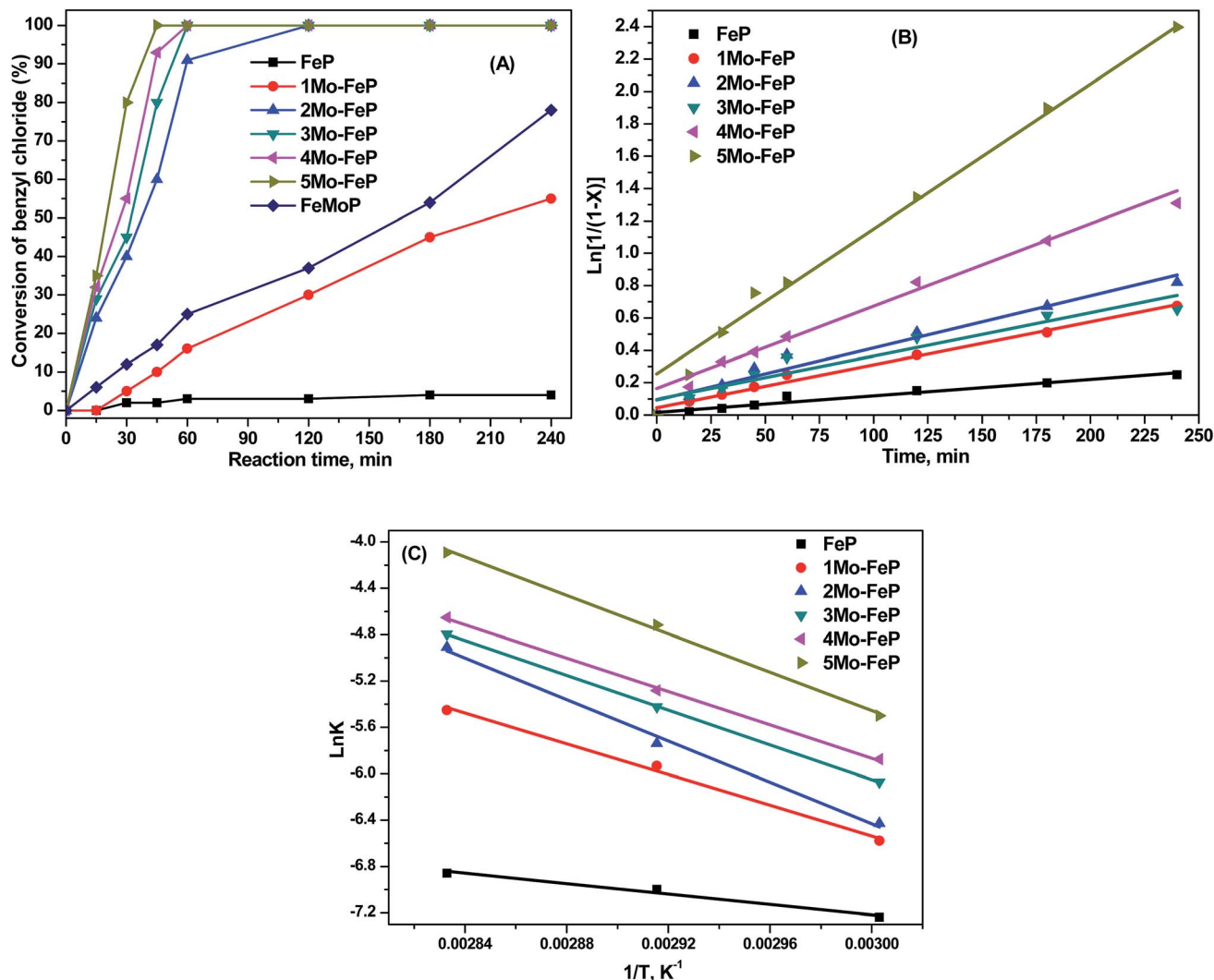


Fig. 8 (A) The conversion of benzyl chloride with the reaction time over FeP, Mo-FeP and FeMoP catalysts, reaction temperature: 80 °C (B) plot of  $\text{Ln}[1/(1-x)]$  as a function of the reaction time over FeP and MoO<sub>x</sub> impregnated FeP catalysts (C) the Arrhenius plots of benzylation reaction for all the catalysts, benzyl chloride : benzene = 1 : 15, wt of catalyst: 50 mg, the selectivity to DPM was varied between 96–98%.

chloride was observed after 15 min. Conversion reached to 100% after a reaction time of 120 min. An increase of Mo loading to 3, 4 and 5 mol% led to further increase in conversion of benzyl chloride. In particular, 5Mo-FeP catalyst offered 100% conversion just after 45 minutes of reaction. The conversion of benzyl chloride profile for bulk FeMoP heteropolyacid salt was included to compare its activity with Mo-FeP catalysts. It is clear that FeMoP showed better conversion than pure FeP and 1Mo-FeP catalysts, but lower than other Mo-FeP composite catalysts. It is also observed that Mo-FeP composite catalysts with higher Mo loading, offer much higher conversion of benzyl chloride after one hour of reaction time.

The kinetic data for the benzylation of benzene in benzene [stoichiometric ratio (benzene/benzyl chloride) = 15] over all the catalysts could be fitted well to a pseudo-first-order rate law:  $\text{Ln}[1/(1-x)] = k_a [t - t_0]$ , where  $k_a$  is the apparent first-order rate constant,  $x$  is the fractional conversion of benzyl chloride,  $t$  is the reaction time and  $t_0$  is the induction period corresponding

to the time required for reaching equilibrium temperature. A plot of  $\text{Ln}[1/(1-x)]$  as a function of time was shown in Fig. 8(B). It is shown in Fig. 8(B) and the data presented in Table S2 (ESI<sup>†</sup>) that the reaction rate constant ' $k_a$ ' for the 5Mo-FeP catalyst is higher than that of pure FeP and twice that of 2Mo-FeP. The turnover frequency (TOF) was estimated based on the mole number of benzyl chloride converted per mole of Mo and Fe species per second. Based on the comparison of the TOF data, it can be seen that the catalytic performance is greater for MoO<sub>x</sub> impregnated FeP catalysts than the FeP, MoO<sub>3</sub> and Fe<sub>2</sub>O<sub>3</sub> materials under the same reaction conditions. For instance, the TOF of 5Mo-FeP is 10 times higher than that of FeP and 30 times than that of MoO<sub>3</sub>. The dependency of TOF on the MoO<sub>x</sub> loading apparently suggests the formation of several MoO<sub>x</sub>-FeP interactive species having different intrinsic activities for the benzylation. In addition, the TOF of bulk FeMoP catalyst was calculated and it is lower than Mo-FeP catalysts except 1Mo-FeP. The selectivity to DPM is very similar for all the catalysts. The obtained products comprised

mainly of DPM (above 96%), with a small amount of DBB (below 4%). Polyaromatic condensation compounds 5 and 6 were not detected in the product analysis.

Friedel–Crafts alkylation is an aromatic electrophilic substitution reaction in which the carbocation is formed by the complexation of alkyl halide with the catalyst. The carbocation attacks the aromatic species for alkylation; hence, the formation of the carbocation is an important step in the reaction mechanism. The activity has significantly increased with the deposition of 1 mol% of Mo loading and the activity increased linearly with the increase of loading from 1 to 5 mol% at 70 °C. However, the conversion of benzyl chloride has reached maximum level (100%) for 2 mol% Mo at 80 °C. To obtain a better insight of the catalysts behaviour, we tested the catalysts with high Mo loadings (3, 4 and 5 mol%) for the benzylation of benzene. These samples also offered 100% conversion with short reaction times at 80 °C. Fig. 8(C) shows the Arrhenius plots of the benzylation for all the catalysts. The observed  $E_a$  values are tabulated in Table S2.† The activation energy for the most active catalysts, 5Mo–FeP and 4Mo–FeP, is 50.5 kJ mol<sup>-1</sup> and 59.8 kJ mol<sup>-1</sup>, respectively. As expected, pure FeP showed a higher activation energy of 78.6 kJ mol<sup>-1</sup>.

The conversion of benzyl chloride and the rate of reaction per unit surface area of FeP and MoO<sub>x</sub> deposited FeP catalysts at different reaction temperatures are presented in Table 3. It is clear that when pure FeP was used as a catalyst, only 22% conversion was observed after 240 min at 70 °C, clearly indicating that the presence of active species is essential to obtain a high conversion in this reaction. The benzyl chloride conversion increased with the increase of the reaction temperature for all the catalysts. In terms of the rates of the benzyl chloride conversion per unit surface area of catalyst, the 5Mo–FeP catalyst showed the highest benzylation reaction rate. The rates per unit surface area were consistent among all catalysts. The greatest difference was observed at high reaction temperature (80 °C), where the 5Mo–FeP catalyst was more active than FeP and other MoO<sub>x</sub> impregnated catalysts. It is interesting to note that bulk FeMoP heteropolyacid salt offered less rates per unit surface area than all of the Mo–FeP catalysts even though it showed more conversion than 1Mo–FeP catalyst. This is due to very low surface area (5 m<sup>2</sup> g<sup>-1</sup>) of the bulk FeMoP catalyst.

A noticeably high difference in activity can be observed in the MoO<sub>x</sub> deposited catalysts with reaction temperature and different compositions; thus, it can be assumed that the catalytic activity of these catalysts in the benzylation of benzene was affected by their content and physico-chemical properties.

Fig. 9(A) illustrates the conversion of benzyl chloride at different reaction temperatures of 60, 70, 80 and 90 °C on the most active catalyst, 5Mo–FeP. It is clear that the 5Mo–FeP sample exhibits significant different catalytic performances in the benzylation of benzene. It can be seen that the conversion levels increased with the increase in reaction temperature. The conversion levels are very low at 60 °C; the maximum conversion is 7% even after 240 minutes. Increasing the reaction temperature to 70 °C resulted in minimal improvement in the conversion levels (11% maximum). However at 80 °C, the conversion was increased to 100% just after 45 min. A similar conversion pattern was observed with a further increase in the reaction temperature of up to 90 °C.

To investigate the effects of the benzyl chloride-to-benzene molar ratio to the most active catalyst 5Mo–FeP, the benzylation experiments were conducted by changing the molar ratio from 1 : 1, 1 : 6 to 1 : 15, while at the same time keeping the reaction temperature and the catalyst amount constant at 80 °C and 50 mg, respectively. Fig. 9(B) demonstrates the effect of the molar ratio of benzyl chloride to benzene on benzyl chloride conversion for the 5Mo–FeP sample. The reaction developed slowly and the 100% conversion was observed in 240 min when molar ratio is 1 : 1. Depending on the different molar ratios of benzyl chloride to benzene, benzylation reached a state of equilibrium at different reaction times. The conversion of benzyl chloride reached 100% at 180 minutes for 1 : 6. It took only 45 minutes to get 100% conversion with a 1 : 15 molar ratio. A similar pattern was observed in the case of other samples; however, the other catalyst requires longer reaction times to convert benzyl chloride. It is known that benzene serves as a solvent as well. An excess of benzene can shift the equilibrium to the right side, improving the conversion of benzyl chloride. The difference in the catalytic activity among the MoO<sub>x</sub> impregnated FeP catalysts is possibly due to the difference in the nature of the interactive species formed between the MoO<sub>x</sub> and FeP in these catalysts.

**Table 3** Conversion of benzyl chloride and reaction rate per unit surface area of FeP and MoO<sub>x</sub> impregnated FeP catalysts at different reaction temperatures<sup>a</sup>

Catalyst	60 °C		70 °C		80 °C	
	Conversion (%)	$\bar{k}$ (min <sup>-1</sup> m <sup>-2</sup> ), 10 <sup>-5</sup>	Conversion (%)	$\bar{k}$ (min <sup>-1</sup> m <sup>-2</sup> ), 10 <sup>-5</sup>	Conversion (%)	$\bar{k}$ (min <sup>-1</sup> m <sup>-2</sup> ), 10 <sup>-5</sup>
FeP	16 (96)	0.40	22 (96)	0.47	23 (96)	0.47
1Mo–FeP	24 (96)	0.49	49 (96)	0.79	63 (96)	2.16
2Mo–FeP	35 (97)	0.72	56 (96)	0.90	99 (96)	3.28
3Mo–FeP	42 (97)	1.31	68 (96)	1.34	99 (96)	4.33
4Mo–FeP	48 (98)	1.53	75 (97)	2.42	99 (96)	5.02
5Mo–FeP	52 (98)	2.78	89 (97)	3.20	100 (97)	5.52
FeMoP	31 (97)	0.42	50 (97)	0.51	78 (97)	1.58

<sup>a</sup> Benzyl chloride : benzene stoichiometric ratio = 1 : 15 and 50 mg of catalyst; the values in parenthesis represents selectivity to DPM.

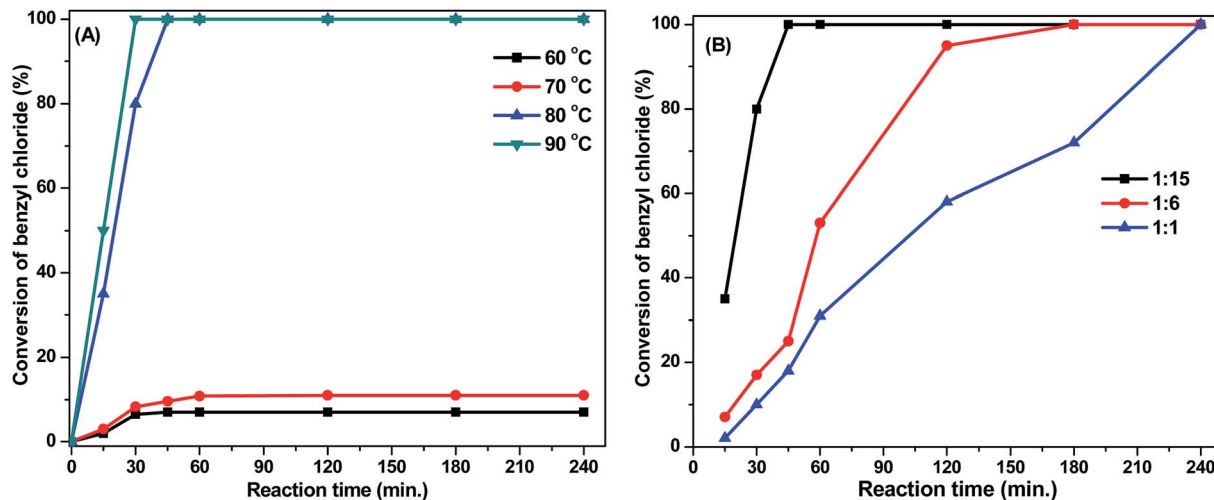


Fig. 9 (A) Conversion of benzyl chloride at different reaction temperatures over 5Mo–FeP (B) effect of molar ratio of benzyl chloride to benzene on benzyl chloride conversion for the 5Mo–FeP sample, reaction temperature: 80 °C, wt of catalyst: 50 mg, the selectivity to DPM was varied between 95–98%.

The obtained characterization results suggest that increasing the amounts of Mo atoms up to 4.4 mol% of Mo, gradually introduced into the FeP framework, have an effect on the Raman, UV-vis spectra, reducibility and acidity of the catalysts. The observed changes unequivocally suggest that Mo atoms in the synthesised materials were introduced into the FeP framework by the breaking of oxygen bridges (*i.e.* P–O–P and Fe–O–P) and the following formation of bonds, such as P–O–Mo and/or Fe–O–Mo. Modifications occurring in the XPS spectra mainly involved the Mo 3d peak, which is not so much assigned for the value of the binding energy (which remained approximately constant for relatively high loading samples), but rather in the form of the peak, which is highly sensitive to the atom environment.<sup>32</sup> On the other hand, it is not possible to easily distinguish between Fe<sup>3+</sup> in the tetrahedral coordination and Fe<sup>3+</sup> in the octahedral coordination by analysis of the Fe 2p peak. Fe<sup>3+</sup> and Fe<sup>2+</sup> in the high-spin state give rise to a multiple effect, which is responsible for peak broadening. However, the Mo 3d peak position provides evidence that the Keggin type species were formed in the case of the 4Mo–FeP and 5Mo–FeP samples.

There are also several reports indicating a decrease in the reducibility of the total catalyst with the increase of active component loading, as well as on the linking of the catalytic activity and selectivity to the reducibility of the catalyst.<sup>33</sup> As the FeMoP heteropolyacid species become more bulk-like; that is, as the particle size increases with an increasing loading, they become more difficult to reduce due to bulk diffusion limitations.<sup>34</sup> This is the reason for the selection of 1 to 5 molar% of Mo. It is clear from our previous study that higher loadings (5 to 25 wt%) of Mo and W produce bulk-like HPA species.<sup>11,19</sup> The H<sub>2</sub>-TPR results clearly indicated that the 5Mo–FeP catalyst can be easily reduced compared to the parent FeP. This may indicate partial reduction of the iron or an increase in the ease of reduction of the MoO<sub>x</sub> deposited FeP.

Comparison of porous nanosized MoO<sub>x</sub>–FePO<sub>4</sub> catalysts with other reported catalysts was tabulated and is presented in Table S3 (ESI<sup>†</sup>). In comparison with previous reports on mesoporous iron based catalysts in the benzylation of benzene with benzyl chloride, 5Mo–FeP catalyst is equally efficient catalyst. It was reported that Fe-MCM-41 (ref. 35) exhibited 90% conversion of benzyl chloride with 95% selectivity towards diphenylmethane; however, this catalyst has a major disadvantage that almost 33% of the iron atoms have been removed from the framework of MCM-41 during reaction cycles. Sun *et al.*<sup>36</sup> reported that 10 wt% iron oxide loaded SBA-15 catalyst showed 100% conversion of benzyl chloride after a reaction time of 30 min and 15 wt% iron oxide loaded SBA-15 gave 100% conversion after a reaction time of 45 min. Leng *et al.*<sup>37</sup> used iron-exchanged mordenite zeolite catalyst for benzylation of benzene by benzyl chloride. The authors observed 100% conversion in just 30 min. However, there are serious questions about the heterogeneous nature and reusability of iron exchanged porous zeolite and SBA-15 catalysts. Shinde and Sawant<sup>38</sup> used various ferrites such as CuFe<sub>2</sub>O<sub>4</sub>, NiFe<sub>2</sub>O<sub>4</sub>, CoFe<sub>2</sub>O<sub>4</sub>, ZnFe<sub>2</sub>O<sub>4</sub>, and MgFe<sub>2</sub>O<sub>4</sub> for benzylation of benzene with benzyl chloride. Among the catalysts, ZnFe<sub>2</sub>O<sub>4</sub> is highly active, which offered 100% conversion of benzyl chloride in 10 min. The authors did not present any data on the selectivity of diphenylmethane, and also the ferrite samples are micropores in nature with low surface area and there is a clear possibility for the diffusional problems. Koyande *et al.*<sup>39</sup> observed maximum 80% of diphenylmethane yield over sulfate-promoted ZrO<sub>2</sub>–Fe<sub>2</sub>O<sub>3</sub> catalyst. It was observed that the activity of the catalyst decreased drastically in the second run itself and suffered gradual loss in activity. Although in the above works the amounts of catalyst and benzyl chloride are different from those used in this work, it can be estimated that 5Mo–FeP is still a very active catalyst in this reaction after the effect factor of amounts of catalyst, reaction time and benzyl chloride is deducted. The main advantage of using porous nanosized

MoO<sub>3</sub>-FePO<sub>4</sub> catalyst in this reaction is its higher hydrothermal and water stability as compared to other mesoporous catalysts; in addition, *in situ* generated FeMoP Keggin species are very difficult to remove from the crystalline framework of iron phosphate.<sup>11</sup>

Reusability is one of the main advantages of heterogeneous catalysts. To test the reusability of Mo deposited FeP catalysts, the benzylation of benzene with benzyl chloride reaction was carried out using 5Mo-FeP catalyst at 80 °C. The conversion levels of the benzyl chloride of this catalyst for five consecutive cycles were determined. The fresh catalyst offered 100% conversion at a reaction time of 45 min correspondingly; the first and second reused catalysts presented exactly the same activity. A slight decrease of conversion (96%) was observed in the third, fourth and fifth cycles. This could be due to the loss of catalyst amount during the reaction recycling. These results indicate that the catalyst could be reused and good activity can be maintained ever after five cycle. Such catalytic performance is of great importance for potential industrial application.

## 4 Conclusions

Nano sized MoO<sub>x</sub>-FeP composites with different Mo molar loadings (1–5%) have been synthesized and used as catalysts for the benzylation of benzene using benzyl chloride. Raman and UV-vis spectroscopic results revealed the formation of a Keggin-like surface structure from the reaction of MoO<sub>x</sub> with exposed PO<sub>4</sub> groups from FeP. H<sub>2</sub>-TPR and acidity measurements indicated that the 5 mol% Mo impregnated FeP catalyst possesses more acidic and easily reducible Keggin type species as opposed to the porous nanosized FeP support and other MoO<sub>x</sub> impregnated samples. All Mo-FeP catalysts showed high activity in the benzylation of benzene with benzyl chloride, with the highest activity observed for 5 mol% of Mo sample. These catalysts are resistant to leaching, are readily recovered and can be recycled without major activity loss.

## Acknowledgements

The authors gratefully thank King Abdulaziz City for Science and Technology (KACST) for the financial support provided through grant no. PS-35-379. The surface chemistry and catalytic studies group at King Abdulaziz University is also acknowledged for the analytical facilities offered and the scientific discussion carried out by the research group.

## References

- G. A. Olah, R. Krishnamurti and G. K. S. Prakash, in *Comprehensive Organic Synthesis*, ed. B. M. Trost and I. Fleming, Pergamon press, Oxford, 1991, vol. III, p. 293.
- R. A. Sheldon, *J. Chem. Technol. Biotechnol.*, 1997, **68**, 381–388.
- P. H. Gore, in *Friedel-Crafts and Related Reactions*, ed. G. A. Olah, Wiley-Interscience, New York, 1964, vol. III.
- T. T. Ali, K. Narasimharao, N. S. Ahmed, S. Basahel, S. Al-Thabaiti and M. Mokhtar, *Appl. Catal., A*, 2014, **486**, 19–31.
- I. V. Kozhevnikov, *Chem. Rev.*, 1998, **98**, 171–198.
- N. Mizuno and M. Misono, *Chem. Rev.*, 1998, **98**, 199–218.
- J. Zhang, Z. Zhu, C. Li, L. Wen and E. Min, *J. Mol. Catal. A: Chem.*, 2003, **198**, 359–367; J. Kaur, K. Griffin, B. Harrison and V. Kozhevnicov, *J. Catal.*, 2002, **208**, 448–455; G. D. Yadav, N. S. Asthana and V. S. Kamble, *J. Catal.*, 2003, **217**, 88–99; B. M. Devassy, S. B. Halligudi, S. G. Hegde, A. B. Halageri and F. Lefebvre, *Chem. Commun.*, 2002, 1074–1075; S. Sarish, B. M. Devassy and S. B. Halligudi, *J. Mol. Catal. A: Chem.*, 2005, **235**, 44–51; B. M. Devassy, G. V. Shanbhag, F. Lefebvre and S. B. Halligudi, *J. Mol. Catal. A: Chem.*, 2004, **210**, 125–134.
- G. Kamalakar, K. Komura, Y. Kubota and Y. Sugi, *J. Chem. Technol. Biotechnol.*, 2006, **81**, 981–988.
- A. S. Tipnis, D. K. Deodhar and S. D. Samant, *Indian J. Chem., Sect. B: Org. Chem. Incl. Med. Chem.*, 2010, **49**, 340–345.
- M. Misono, *J. Chem. Soc., Chem. Commun.*, 2001, 1141–1152.
- C. Srilakshmi, K. Narasimharao, N. Lingaiah, I. Suryanarayana and P. S. Sai Prasad, *Catal. Lett.*, 2002, **83**, 127–132.
- D. Yu, J. Qian, N. Xue, D. Zhang, C. Wang, X. Guo, W. Ding and Y. Chen, *Langmuir*, 2007, **23**, 382–386.
- X. Wang, Y. Wang, Q. Tang, Q. Guo, Q. Zhang and H. Wan, *J. Catal.*, 2003, **217**, 457–467.
- P. Nagaraju, C. Srilakshmi, N. Pasha, N. Lingaiah, I. Suryanarayana and P. S. S. Prasad, *Appl. Catal., A*, 2008, **334**, 10–19.
- C. Rocchiccioli-Deltcheff, R. Thouvenot and R. Frank, *Spectrochim. Acta, Part A*, 1976, **32**, 587–597.
- D. H. Yu, J. S. Qian, N. H. Xue, D. Y. Zhang, C. Y. Wang, X. F. Guo, W. P. Ding and Y. Chen, *Langmuir*, 2006, **23**, 382–386.
- M. Roy, H. Ponceblanc and J. C. Volta, *Top. Catal.*, 2000, **11–12**, 101–109.
- A. Cotton, E. G. Wilkinson, C. A. Murillo and M. Bochmann, *Advanced Inorganic Chemistry*, Wiley-Interscience, New York, 6th edn, 1999.
- K. Narasimharao, A. Sridhar, A. F. Lee, S. J. Tavener, N. A. Young and K. Wilson, *Green Chem.*, 2006, **8**, 790–797.
- G. O. Alptekin, A. M. Herring, T. R. Ohno, D. L. Williamson and R. L. McCormick, *J. Catal.*, 1999, **181**, 104–112.
- Y. Wang and K. Otsuka, *J. Catal.*, 1996, **161**, 198–205.
- J. Moulder, W. Stickle, P. Sobol and K. Bomben, *Handbook of X-ray Photoelectron Spectroscopy*, Perkin-Elmer, 1992.
- M. Zhang, L.-F. Jiao, H.-T. Yuan, Y.-M. Wang, J. Guo, M. Zhao, W. Wang and X.-D. Zhou, *Solid State Ionics*, 2006, **177**, 3309–3314.
- S. Damyanova, M. L. Cubeiro and J. L. G. Fierro, *J. Mol. Catal. A: Chem.*, 1999, **142**, 85–100.
- R. K. Brow, C. M. Arens, X. Yu and E. Day, *Phys. Chem. Glasses*, 1994, **35**, 132–136.
- M. Langpape, J. M. M. Millet, U. S. Ozkan and M. Boudeulle, *J. Catal.*, 1999, **181**, 80–90.
- G. W. Coulston, E. A. Thompson and N. Herron, *J. Catal.*, 1996, **163**, 122–129.
- S. J. Gregg and K. S. W. Sing, *Adsorption, Surface Area and Porosity*, Academic Press, London, 2nd edn, 1982.

- 29 D. J. Rensel, S. Rouvimov, M. E. Gin and J. C. Hicks, *J. Catal.*, 2013, **305**, 256–263.
- 30 I. Rossetti, C. Biffi, C. L. Bianchi, V. Nicheleb, M. Signoretto, F. Menegazzo, E. Finocchio, G. Ramis and A. Di Michele, *Appl. Catal., B*, 2012, **117–118**, 384–396.
- 31 S. M. Kumbar, G. V. Shanbhag, F. Lefebvre and S. B. Halligudi, *J. Mol. Catal. A: Chem.*, 2006, **256**, 324–334.
- 32 E. Etienne, F. Cavani, R. Mezzogori, F. Trifirò, G. Calestani, L. Gengembre and M. Guelton, *Appl. Catal., A*, 2003, **256**, 275–290.
- 33 M. B. Reddy, K. Narasimha, P. Kanta Rao and V. M. Mastikhin, *J. Catal.*, 1989, **118**, 22–30.
- 34 M. M. Koranne, J. C. Goodwin and G. Marcelin, *J. Catal.*, 1994, **148**, 378–387.
- 35 A. Arafat and Y. Alhamed, *J. Porous Mater.*, 2009, **16**, 565–572.
- 36 Y. Sun, S. J. Walspurger, P. Tessonnier, B. Louis and J. Sommer, *Appl. Catal., A*, 2006, **300**, 1–7.
- 37 K. Leng, S. Sun, B. Wang, L. Sun, W. Xu and Y. Sun, *Catal. Commun.*, 2012, **28**, 64–68.
- 38 M. M. Shinde and M. R. Sawant, *J. Chin. Chem. Soc.*, 2003, **50**, 1221–1226.
- 39 S. N. Koyande, R. G. Jaiswal and R. V. Jayaram, *Ind. Eng. Chem. Res.*, 1998, **37**, 908–913.